Jets and Bipolar Outflows from Young Stars: Theory and Observational Tests

Hsien Shang
Institute of Astronomy and Astrophysics, Academia Sinica

Zhi-Yun Li
University of Virginia, Charlottesville

Naomi Hirano
Institute of Astronomy and Astrophysics, Academia Sinica

Jets and outflows from young stars are an integral part of the star formation process. A particular framework for explaining these phenomena is the X-wind theory. Since PPIV, we have made good progress in modeling the jet phenomena and their associated fundamental physical processes, in both deeply embedded Class I objects and more revealed classical T Tauri stars. In particular, we have improved the treatment of the atomic physics and chemistry for modeling jet emission, including reaction rates and interaction cross-sections, as well as ambipolar diffusion between ions and neutrals. We have broadened the original X-wind picture to include the winds driven magnetocentrifugally from the innermost disk regions. We have carried numerical simulations that follow the wind evolution from the launching surface to large, observable distances. The interaction between the magnetocentrifugal wind and a realistic ambient medium was also investigated. It allows us to generalize the shell model of *Shu et al.* (1991) to unify the the jet-driven and wind-driven scenarios for molecular outflow production. In addition, we review related theoretical works on jets and outflows from young stars, and make connection between theory and recent observations, particularly those from HST/STIS, VLA and SMA.

1. INTRODUCTION

Jets and outflows have long been recognized as an important part of star formation. They are reviewed in both PPIII and PPIV, and by several groups in this volume (*Bally et al.*, *Arce et al.*, *Pudritz et al.*, *Ray et al.*). Our emphasis will be on the X-wind theory and related work, and connection to recent high resolution observations. Comparisons with other efforts are made where appropriate.

Since PPIV, progress has been made in modeling both the dynamics and radiative signatures of jets and winds. There is increasing consensus that these outflows are driven by rotating magnetic fields, although many details remain unresolved. The old debate between disk winds (*Königl and Pudritz*, 2000) and X-winds (*Shu et al.*, 2000) is still with us. Ultimately, observations must be used to distinguish these and other possibilities. Predicting the radiative signatures of different dynamical models is a key step toward this goal. This effort is reviewed in the first part of the Chapter (Section 2 through Section 5).

The X-winds and disk winds are not mutually exclusive. Both are driven magnetocentrifugally from open field lines anchored on rapidly rotating circumstellar disks. Their main distinction lies in where the field lines are anchored: near the radius of magnetospherical truncation on the disk – the X-point – for X-winds and over a wider range in disk radii for disk winds. The different outflow launching conditions envisioned in these scenarios cannot yet be probed directly by observations. It is prudent to consider both possibilities. An effort in this direction is numerical simulation of winds driven magnetocentrifugally from inner disk regions over a range in disk radii that is adjustable. The results of this effort are summarized in the second part of the Chapter (Section 6), which also includes a method for locating the footpoints of wind-launching magnetic field lines on the disk based on measurements of rotation speed at large distances (Section 7).

Regardless of where a magnetocentrifugal wind is driven, as long as its launching region is much smaller than the region of interest, its density structure asymptotes to a characteristic distribution: nearly cylindrical stratification, first shown by *Shu et al.* (1995). An implication is that a magnetocentrifugal wind naturally has dual characters: a dense axial jet, surrounded by a wide-angle wind. This intrinsic structure provides a basis for unifying the jet-driven and wind-driven scenarios of molecular outflows, which are thought to be mainly the ambient material set into motion by the primary wind. We devote the last part of the review to recent theoretical and observational advances in this direction (Section 8 and Section 9). Concluding remarks are given in Section 10.

2. THERMAL-CHEMICAL MODELING OF X-WINDS

Thermal-chemical modeling of the winds of young stellar objects is an important step towards understanding their dynamics and origins. *Ruden, Glassgold, and Shu* (1990; hereafter RGS) was the first to investigate in detail the thermal and ionization structure of a cold spherical wind. *Safier* (1993a) implemented similar chemistry into a self-similar disk-wind (a model generalizing the solution of *Blandford and Payne*, 1982). *Shang et al.* (2002, SGSL) extended and improved upon previous chemical and physical processes of RGS to establish a package of diagnostic tools based on the X-wind. Concurrently, *Garcia et al.*, (2001a,b) extended the work of *Safier* (1993a,b) by computing the thermal and ionization structure of the self-similar disk-winds of *Ferreira* (1997). The advances in thermal-chemical modeling since PPIV, particularly SGSL, are reviewed below.

2.1 Basic Formulation

Many processes are involved in determining the thermal and ionization structure of jets. SGSL considered both processes that take place locally in the wind, and external contributions from mechanical disturbances and radiation on top of the background smooth flow, including new ingredients such as UV radiation and photo-ionization from the accretion hot spots where the funnel flows strike the stellar surfaces, and ionization and heating by X-rays from the secondary electrons. We begin by describing the basic formulation of the problem.

The temperature T and electron fraction $x_{\rm e}$ of a steady flow are governed by the rate equations that balance heating and cooling and ionization production and destruction. The ionization is primarily destroyed by radiative recombination. Recombination and adiabatic cooling set the two basic timescales in the flow. The former is long compared to flow time and the latter is only tens of seconds near the base. Adiabatic expansion cooling has been recognized as a "severe constraint" on potential heat sources independent of details of wind models (RGS). The balance of heating and cooling due to adiabatic expansion provides a rough estimate for the asymptotic temperature profile. In RGS, ambipolar diffusion was the dominant heat source; while in SGSL, other mechanical contributions play more important roles (Section 2.4).

The hydrogen-based radiative and collisional processes that take place locally in a fluid element form the background network of reactions. These are ionization by Balmer continuum, H^- detachment, and collisional ionization; heating by ambipolar diffusion, Balmer photoionization of H, H^++H^- neutralization, and H^- photodetachment; cooling by H^- radiative attachment, recombination of H^+, Lyα, collisional ionization, and line cooling from the heavy elements. The chemistry that form and dissociate hydrogen molecules may enter the network if the wind is predominantly molecular; however, bright optical jets can be reasonably treated as atomic winds. Table 1 of SGSL has a summary of processes mentioned above.

The rate coefficients of most atomic processes were improved in SGSL. For example, the rate coefficient of the reaction $H^- + H^+ \rightarrow H(1) + H(n)$ was revised in light of newer measurements. Photo-rates involving photodetachment of H^- were computed with better approximations. The electronic collisions and X-ray ionization affect the level population of atomic hydrogen at $n = 2$. The presence of X-rays also causes an indirect contribution of heating, in addition to the direct heating by elastic collisions of H atoms at the $n = 2$ level with X-rays. These enter when detailed processes involving the levels $n = 1$ and 2, and the continuum are considered.

2.2 Effects of X-Rays

The effects of X-rays on the disk surrounding a young star have been reviewed in *Glassgold et al.* (2000, 2005b), and the chapter by *Najita at al.* in PPV. Before reaching the outer part of the disk, the X-rays may first intercept and interact with a wind. SGSL considered the effects of X-rays on an X-wind using an approach similar to that developed for X-ray irradiated disks.

In an X-wind environment, a useful estimate for the X-ray ionization rate $\zeta_{\rm X}$ at a distance $r = R_{\rm x}$ (the distance of X-point to the star, effectively the base of the X-wind) from a source of X-ray luminosity $L_{\rm X}$ can be expressed as

$$\zeta_{\rm X} \equiv \frac{L_X \sigma_{\rm pe}(kT_{\rm X})}{4\pi R_{\rm x}^2 kT_{\rm X}} = 1.13\times10^{-8}{\rm s}^{-1}\left(\frac{L_X}{10^{30}{\rm ergs}^{-1}}\right)\left(\frac{kT_{\rm X}}{\rm keV}\right)^{-(p+1)}\left(\frac{10^{12}{\rm cm}}{R_{\rm x}}\right)^2, \quad (1)$$

for a thermal spectrum of temperature $T_{\rm X}$ for the X-rays, where $\sigma_{\rm pe}$ is the energy-smoothed cosmic photoelectric absorption cross section per H nucleus. The ionization rate ζ at a distance r from the X-ray source can be further expressed with respect to the rate at the X-point as

$$\zeta \approx \zeta_{\rm X}\left(\frac{R_{\rm x}}{r}\right)^2\left(\frac{kT_{\rm X}}{\epsilon_{\rm ion}}\right) I_p(\tau_{\rm X},\xi_0), \quad (2)$$

where $\epsilon_{\rm ion}$ is the energy to make an ion pair, and the function $I_p(\tau_{\rm X},\xi_0)$ describes the attenuation of the X-rays in the surrounding medium, which is a sensitive function of the X-ray optical depth $\tau_{\rm X}$ calculated from the low-energy cutoff ξ_0 expressed in temperature units (see also *Glassgold et al.*, 1997; SGSL).

X-rays are capable of lightly ionizing the innermost jet proper and the base of the wind for typical X-ray luminosities observed in young stars through *Chandra* (e.g., *Feigelson et al.*, 2002, 2005, chapter in this volume) and earlier satellite missions *ASCA* and *ROSAT* (e.g., *Feigelson and Montmerle*, 1999). Together with UV photons from accretion hot spots, they can quantitatively account for the majority of the ionization at the base of the flow. The recombination time scale for an X-wind is long compared to the

flow time for the bulk of the flow volume. Hence ionization created locally (in a Lagrangian frame) could be preserved and carried by the flow to large distances. Because of the $1/r^2$ drop-off in the ionization parameter ζ (Eqn.[2]), and the peculiar $1/\varpi^2$ profile of the density (where ϖ is horizontal distance to the axis), the ionization rate is a slowly attenuated function in winds that are not very optically thick. Within the X-wind framework, X-rays can effectively ionize the inner jet throughout a hollow cone that is supported by an axially opened stellar magnetic field. At an elevated angle geometrically over the base of the X-wind, the ionizing X-rays would be less absorbed when the paths of rays go through the diverging portion of the flow.

The effective ionizing power scales approximately as $L_{\rm X}/\dot{M}_{\rm w}$ since the ionization rate enters the rate equation as $\zeta/n_{\rm H}$ (where $n_{\rm H}$ is the volumetric density of hydrogen nuclei), when no other competitive processes are present. The ratio $L_{\rm X}/\dot{M}_{\rm w}$ can be interpreted as the *average* efficiency for converting accretion power into X-rays at radius $R_{\rm x}$: $L_{\rm X}/\dot{M}_{\rm w} = \epsilon_{\rm X} GM_*/fR_{\rm x}$ (*Shu et al.*, 1997). The small factor $\epsilon_{\rm X}$ measures the efficiency of converting accretion energy into X-rays, if the energetic events of X-ray production are ultimately powered by accretion through the twisted field lines between the star and the disk. For models where X-rays are capable of maintaining ionization fractions of a few to several percent at physical distances of interest to optical forbidden lines, the level of $L_{\rm X}$ needed may go up to $10^{31} - 10^{33}$ erg/s. Although on the high end of the distribution of flare luminosity for typical Class I-II sources, such a level of X-ray luminosity has been seen in giant flares from protostars (chapter by *Feigelson et al.*; e.g., *Tsuboi et al.*, 2000; *Grosso et al.*, 1997). For lower luminosity objects, additional sources of ionization must be sought (see Section 2.4 below).

2.3 Ambipolar Diffusion

RGS was the first to consider wind heating due to ambipolar diffusion carefully. The authors adopted a spherically symmetric wind model, with profiles of density, velocity and Lorentz forces chosen such that the neutrals were accelerated to escape velocity by the ion-neutral drag. They concluded that the ambipolar diffusion associated with the magnetic acceleration was the dominant heating process, and adiabatic expansion the dominant cooling process. The wind plasma was lightly ionized ($< 10^{-4}$) and cooled below 100 K at a distance beyond 10^4 times the stellar radius. Such conditions were unfavorable for optical emission in the predominantly atomic winds. Based on similar chemistry and atomic processes, *Safier* (1993a) found on the contrary that ambipolar diffusion was in fact capable of heating a self-similar disk wind easily to 10^4K, with an electron fraction as high as $\sim 0.1 - 1$ at distances of $\sim 10^2 - 10^3$ AU from the central star. The discrepancy is not completely resolved with an improved treatment of ambipolar diffusion (see below).

There are some uncertainties in computing the heating rate of ambipolar diffusion. The rate is given approximately by (SGSL, eq.[4.1] and [4.2]):

$$\Gamma_{\rm AD} = \frac{\rho_{\rm n}|\mathbf{f}_{\rm L}|^2}{\gamma\rho_{\rm i}(\rho_{\rm n}+\rho_{\rm i})^2}, f_L = \frac{1}{4\pi}(\nabla\times\mathbf{B})\times\mathbf{B}, \qquad (3)$$

where ρ_n and ρ_i are the mass densities of the neutrals and the ions, respectively, and f_L the Lorentz force. When $\rho_i \ll \rho_n$, equation (3) reduces to the usual one for low-ionization situations, e.g., Eq. (27.19) of *Shu* (1992). It has the important property that when ρ_n vanishes the heating rate $\Gamma_{\rm AD}$ goes to zero.

The ion-neutral momentum transfer coefficient, γ, plays the central role of determining the numerical values of ambipolar diffusion heating in different regimes. SGSL combined previous approximations by *Draine* (1980), and adopted updated calculations and experiments on the collision of H^+ ions with atomic and molecular hydrogen and with helium. The exchange scattering in H^+ + H collisions from *Krstić and Schultz* (1998) was included as the sum of contributions from power-laws from both the high- and low-energy regimes. It agrees with Draine's prescription (1980) only for cold clouds.

Glassgold et al. (2005a) re-investigated the adopted forms of γ and numerical values in different energy regimes through quantum mechanical calculations of H^+ scattering by H. They fit the coefficient down to very low energy (10^{-10} ev), and did not find the traditional behavior of $1/v$ expected from a constant Langevin cross section. They showed that the early fit of *Draine* (1980) remains accurate within 15%-25%, whereas the approximation adopted by SGSL (their Eqn. [4.3]) is too big by a factor of 2. The overestimate came from the assumption that the rate coefficient tends to the Langevin rate at low velocities adopted by astrophysicists (e.g., *Osterbrock*, 1961). After dropping the contribution from the assumed Langevin behavior, the revised formula that *Glassgold et al.* (2005a) suggested SGSL should have adopted can be used to a good approximation (Eqn. [3.20] in *Glassgold et al.*, 2005a).

SGSL concluded that ambipolar diffusion cannot heat an X-wind in an extended volume up to the temperature of $\sim 10^4$ K and ionization fraction $x_e \sim 0.01$ or higher inferred from forbidden optical lines. Even with a better wind configuration and magnetic field geometry, their conclusion on ambipolar diffusion agrees with the earlier RGS findings. Adopting the revised value of γ suggested by *Glassgold et al.* (2005a) does not change this conclusion. *Garcia et al.* (2001a), on the other hand, reached the same conclusion as *Safier* (1993a) that ambipolar diffusion is able to heat a self-similar disk wind to a temperature plateau $\simeq 10^4$K. However, they obtained a very different profile of ionization fraction, a factor of 10 down from Safier (1993a). The difference was attributed to the omission of thermal velocity in the ion-neutral momentum-exchange rates adopted by *Safier* (1993a), which overproduced the electron fraction (*Garcia et al.*, 2001a) while making no obvious change in temperature. The systematic disagreement in the heating of self-similar disk winds and non-heating of X-winds may be

related to the difference in the the exact configurations of the magnetic field throughout the wind, although detailed comparative studies are needed to quantify this possibility (*Garcia et al.*, 2001a; *Glassgold et al.*, 2005a).

2.4 Mechanical Heating and Ionization

To mimic the effects of time-variabilities often seen in knotty jets, we adopt here a phenomenological expression for the volumetric rate of mechanical heating (Eqn. [5-2] of SGSL):

$$\Gamma_{\rm mech} = \alpha\,\rho\frac{v^3}{s}. \tag{4}$$

where ρ and v are the local gas density and flow velocity in an inertial frame at rest with respect to the central star, and s is the distance that the fluid element has traveled along a streamline in the flow. The *global* coefficient $\alpha \geq 0$ phenomenologically characterizes the *average* magnitude of disturbances, possibly magnetic in origins. A choice of $\alpha \ll 1$ indicates that only a small fraction of the mechanical energy contained in the shock waves and turbulent cascades is dissipated into heat when integrated over the flow volumes of interest at the characteristic distance s. Small values of α are self-consistent for a cold flow. In the regime of weak disturbances, the variabilities can be treated as small perturbations on top of a more steady background flow.

An averaged estimate of α is simply adopted for modeling purposes. In real systems, the local efficiency of dissipation may determine an α for each fluid element. For strong disturbances, α should be very localized in nature. This approach is partly motivated by the knotty appearance of jets, which indicates time-variabilities in the systems. For example, an $\alpha \approx 0.002$ adopted in SGSL for a slightly revealed source suggests a variation in velocity of less than 5%. Given a typical jet velocity of 300 km/s, this implies a weak shock of 15 km/s decaying over the jet length $\sim s$. The thermal profiles generated by all the physical processes included are consistent with the underlying dynamical properties, stellar parameters, chemistry, heating and ionizing sources in the framework of star-disk interacting systems.

The shock waves represented in equation (4) can also produce UV radiation in the Balmer and Lyman continua that ionize as well as heat the gas. In the same spirit, we can express a phenomenological ionization rate per unit volume (*Shang et al.*, 2004; hereafter SLGS):

$$P_e = \beta n_H v/s, \tag{5}$$

where β is the shock-ionization parameter. If the local medium is optically thin to UV radiation, the simplest way to ionize locally is to convert mechanical input into UV photons. This perhaps can help explain some local increase in ionization fraction, in addition to collisional ionization.

3. FORBIDDEN EMISSION LINES

Thermal-chemical modeling helps to bring theoretical wind models to confront observations. Predictions of the images, position-velocity diagrams, and diagnostic line ratios (Section 3.1 and Section 3.2) are most useful to infer emission properties from comparison with observations of bright jets of young stars. For young active Class I-II sources, red forbidden lines [SII], [OI], and [NII] are most commonly observed. The modeling of their properties based on physical conditions arising in the X-wind is described here.

The ionizations created by X-rays and UV photons and temperature raised by mechanical heating set the overall excitation profiles of X-winds. The general pattern of ionization along the length of jets produced in SGSL resembles a trend seen in optical jets from high resolution observations (e.g., *Bacciotti and Eislöffel*, 1999, hereafter BE; *Bacciotti*, 2002): the electron fraction first rises, then decays along the length of jets following roughly the behavior determined by recombination. The highest values of ionization fraction inferred from the bases of jets are close to $\sim$ 30-60% (e.g., *Lavalley-Fouquet et al.*, 2000; *Bacciotti*, 2002). Overall, the ranges obtained from model calculations are within the observational findings of 1-60% throughout the lengths of jets (e.g., *Ray and Bacciotti*, 2003). To excite optical forbidden lines to the observed level of fluxes and spatial extents, enough emitting volume (and area) of gas needs to be heated to temperature of $\gtrsim 8,000 - 10,000$ K. This poses a constraint for the minimal average value of the parameter α for specific X-wind parameters. (For a review on the units of scaling adopted within X-wind models, readers can refer to *Shu et al.*, 2000)

Synthetic images best deliver the direct visual effects of emission predicted from models. The local excitation condition expressed in the electron fraction x_e and temperature T and cylindrically stratified density distribution of the wind determines the radiative properties that characterize the source. Fig. 1(a) shows the distributions of electron fractional abundance x_e and temperature T in a representative X-wind solution calculated in SGSL for an active revealed source. Fig. 1(b) shows the synthetic images made in [SII] and [OI] lines. Note that the emission fans out near the base of the jet, giving an impression of a conic opening near the base. The appearance differs substantially from that of isodensity contours, which is strictly cylindrical in the model (Figs. 1 and 2 in *Shang et al.*, 1998). This example illustrates the importance of computing the excitation conditions self-consistently. They play a crucial role in determining how a jet is perceived. The main effect of heating is to change the excitation conditions of the background flow, which could be roughly modeled by steady-state solutions. The synthetic images of X-winds obtained with detailed treatment of excitation conditions strengthen the notion, put forth originally in *Shu et al.* (1995), that observed jets are merely "optical illusion".

3.1 Optical Diagnostics

Bright optical emission lines are the best candidates to diagnose conditions arising in real jets and wind mod-

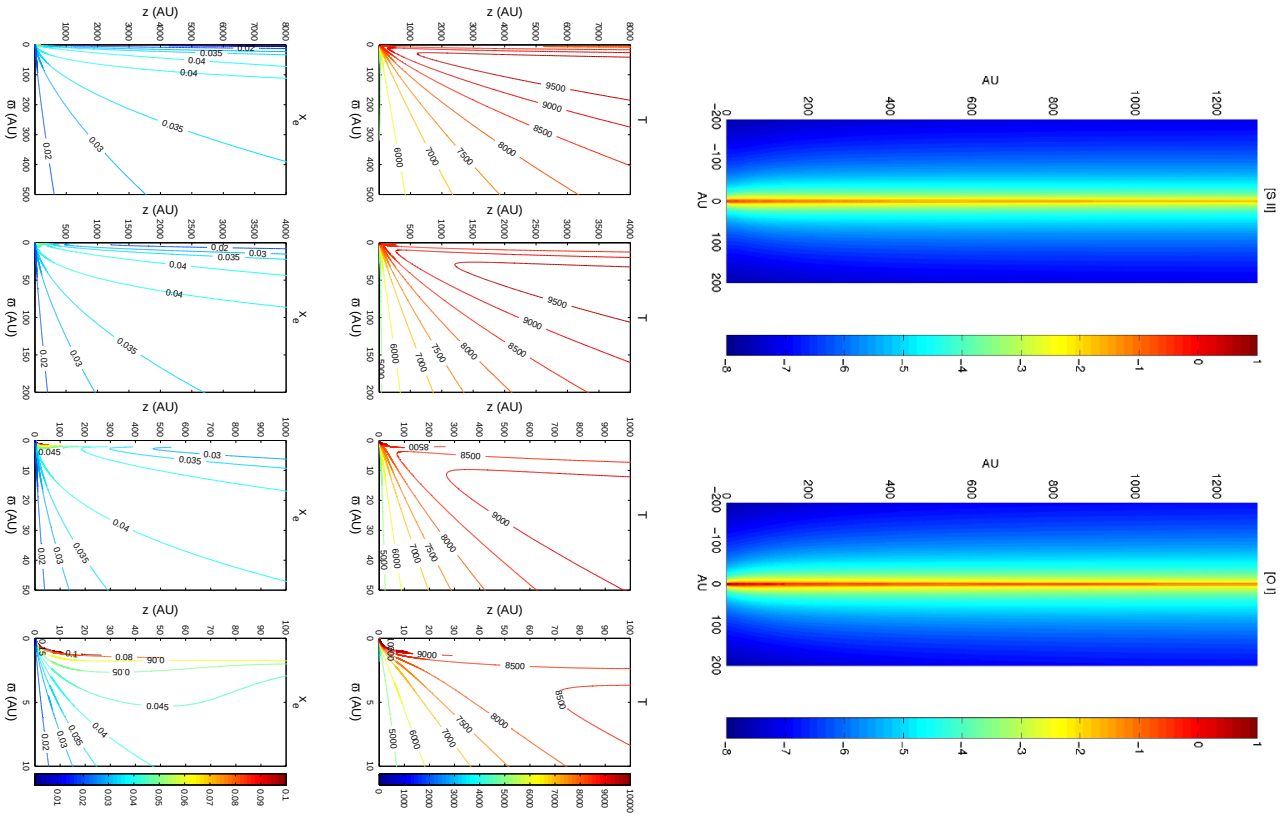

Fig. 1.— (a), *Left*: Temperature (upper) and ionization (lower) contours in the $\varpi - z$ plane calculated in SGSL for a fiducial case characterizing an active but revealed source. The mass loss rate adopted is $3 \times 10^{-8} M_{\odot}$/yr, and $L_{\rm X}/\dot{M}_w = 2 \times 10^{13}$ erg/g for a X-ray luminosity $L_{\rm X} = 4 \times 10^{31}$ erg/s. The parameter α is 0.002 with no inclusion of β in the case shown. The units for the spatial scales are AU. (b) Synthetic images of the [SII]λ6731 (left) and [OI]λ6300 (right) brightness for the same model as in (a) adapting the methods of *Shang et al.* (1998). The $\log_{10}$ of integrated intensity is plotted in units of erg s^{-1} cm^{-2} ster^{-1}.

els. Important constraints can be extracted from the relative strengths of the optical forbidden lines, with knowledge of their individual atomic structures, and physical processes of excitation and de-excitation. BE developed a semi-experimental approach that has been widely applied to available HST and Adaptive Optics data. The so-called BE technique is based on some simple assumptions. The jet emitting region is optically thin. The electron fraction x_e is determined solely by charge exchange with N and O. Collisional ionization and photo-ionization (via shocks) do not contribute until shock velocity exceeds 100 km/s. Sulfur is singly ionized because of its low first ionization potential. The ratio of [SII] doublets $\lambda6717$ and $\lambda6731$ can be used as a density indicator of n_e up to 2×10^4 cm^{-3}, if the two sulfur doublets are treated as a two-level system. The ratio of [OI]($\lambda6300 + \lambda6363$) and [NII]($\lambda6548 + \lambda6583$) and that of [SII]($\lambda6717 + \lambda6731$) and [OI] ($\lambda6300 + \lambda6363$) are tracers of the electron fraction x_e and temperature T_e, respectively. The background abundances of each of the atomic species are assumed to be solar: N/H=1.1×10^{-4}, O/H=6.0×10^{-4}, and S/H=1.6×10^{-5}. There was no implicit assumption made for the excitation mechanisms, although some uncertainties exist in the atomic and ionic physics used in BE. Applying BE to bright jet sources typically yields $0.01 < x_e < 0.6$, and $7000 < T_e < 2 \times 10^4$ (see the chapter by *Ray et al.* for more detailed discussions). The total hydrogen nuclei $n_{\rm H}$ is derived using the upper limit of $n_e = 2 \times 10^4$ cm^{-3} for the sulfur doublets and the inferred electron fraction x_e (*Bacciotti*, 2002). Similar analyses extended to IR or semi-permitted UV lines from the same or different species, could provide independent checks on the derived parameters ($n_e, x_e, T_e, n_{\rm H}$) and the mass loss rates.

Cross-correlation of different lines can reveal interesting trends in the underlying physical conditions of jets. *Dougados et al.* (2000, 2002) used diagrams of relative line strengths to infer physical conditions in strong micro-jets DG Tau and RW Aur (e.g., Fig. 4 of *Dougados et al.*, 2002). They found that the line ratio [NII]/[OI] increases with x_e, [SII]/[OI] decreases with increasing electron temperature and electron density for $n_e \geq n_{\rm cr}$, the critical density. The observational data were compared with the predictions of a few models. Planar shocks (*Hartigan et al.*, 1994) trace a family of curves in the [SII]($\lambda6717/\lambda6731$)-[SII]/[OI] diagram. Shock curves for different pre-shock densities are distinctly separated out on the [NII]/[OI]-[SII]/[OI] diagram. Curves from viscous mixing layers with neutral boundaries (*Binette et al.*, 1999) and a version of the cold disk-wind model heated by ambipolar diffusion (*Garcia et al.*, 2001a,b) follow trajectories on the diagrams that are distinct from those of shock models. On the same diagrams, Herbig-Haro objects obtained by ground-based telescopes (*Raga et al.*, 1996) follow closely shock curves of pre-shock density $10^2 - 10^3$ cm^{-3}

Line ratio diagrams have been used to constrain the X-wind model. SGSL constructed a line ratio diagram of [SII]$\lambda6716$/[SII]$\lambda6731$ and [SII]$\lambda6731$/[OI]$\lambda6300$ for an X-wind jet of mass loss rate $3 \times 10^{-8} M_\odot$/yr, using model data points from the images shown in Fig. (1b). Observational data for the HH objects studied in *Raga et al.* (1996), and DG Tau (from Fig. 3 of *Lavalley-Fouquet et al.*, 2000) are plotted on the same diagram for comparison. AO data for RW Aur (*Dougados et al.*, 2002) would also be located within the coverage of the model points. The model points encompass most of the observational data. With only a few sources, which are known to be strong shock excited objects (in knots or bow shocks), lying outside of the loci traced by the shape of potential curves, the distribution of physical and excitation conditions reached in an X-wind jet for a slightly revealed source indeed captures the average conditions inferred from optical jets.

From the comparison of theoretical and observational data, SGSL concluded that the treatment of weak shocks on top of a steady-state background flow appears to recover the excitation conditions inferred from a large set of optical jets and HH objects. The dynamical properties in fact remain close to the cold steady state solution of the underlying X-wind model. The wide range in shock conditions inferred in the jets may not be a coincidence. Most optical emission, excited by a network of weak shocks, may be the tell-tale traces of vastly varying density structures that cannot be observationally resolved with the current instrumentation, but whose presence can be inferred from detailed modeling.

3.2 Infrared Diagnostics

Compared to optical emission, the near-IR lines have the obvious advantage of being less affected by extinction (*Reipurth et al.*, 2000). However, their radiative properties have not been theoretically explored as thoroughly. Strong near-IR lines of the abundant ion [FeII] are frequently associated with Class I sources or revealed T-Tauri sources of relatively high mass accretion rates (*Davis et al.*, 2003). Sources showing strong [FeII] and optical forbidden lines such as L1551-IRS5 (*Pyo et al.*, 2002, 2005a) and DG Tau (*Pyo et al.*, 2003) have been well studied observationally at both wavelengths. RW Aur and HL Tau have recently been studied by the Subaru telescope with spectroscopy and adaptive optics (*Pyo et al.*, 2005b), adding to the list of sources available for multi-line modeling.

The [FeII] ion has hundreds of fine structure levels. The large number of possible transitions between the levels makes the calculation of level populations a daunting task. Most atomic data and radiative coefficients of [FeII] were not available until after the mid-90's. *Zhang and Pradhan* (1995) included 142 fine-structure levels for transitions in IR, optical, and UV, and 10011 transitions were calculated. *Hartigan et al.* (2004) included 159 energy levels and 1488 transitions for coverage of wavelengths longer than 8000Å. For the purpose of modeling only cooler regions of jets and [FeII] in the near-IR, a simplified non-LTE model for the lowest 16 levels under the optically thin assumption may provide a reasonable approximation, as shown in *Pesenti et al.* (2003). The level populations are computed under sta-

tistical equilibrium with electron collisional excitation and spontaneous radiative emission processes. The lowest levels of the [FeII] ion may remain collisionally dominated as suggested by *Verner et al.* (2000) as in the case of Orion Nebula. For the brightest lines whose ratios are to be taken, results from *Pesenti et al.* (2003) and *Pradhan and Zhang* (1993) agree well for n_e ranging from 10 to 10^8 cm^{-3} and temperature from 3000 to 2×10^4K.

Critical densities derived from the forbidden lines are often used to infer densities from which the radiation originates. The [FeII] near-IR lines have critical densities in the range of $\sim 10^4 - 10^5$ cm^{-3} for temperature up to 10^4 K (Table 1 in *Pesenti et al.*, 2003), sitting between the critical densities of [SII] ($\sim 10^3$ cm^{-3} from 16 levels) and [OI] ($\sim 10^6$ cm^{-3}). The ratio of the two brightest lines, [FeII]1.644 μm and 1.533 μm can be a diagnostic for n_e in the range $\sim 10^2 - 10^5$ cm^{-3}. This may be combined with bright transitions in the red (0.8617 and 0.8892 μm) to derive an estimate on temperature (*Nisini et al.*, 2002a). *Pesenti et al.* (2003) proposed a line-ratio diagram based on the correlation between 1.644μm/1.533μm and 0.8617μm/1.257μm (Fig. 3 in *Pesenti et al.*, 2003). *Nisini et al.* (2005) adopted 1.644μm/1.533μm and 1.644μm/0.862μm as their diagnostic diagram (Fig. 6 in *Nisini et al.*, 2005). (Note: the notation of lines in this section Section 3.2 is changed from the optical diagnostics in Section 3.1 to follow the standard practice of the infrared diagnostics for easier identification with literature.)

Multiline analysis across accessible wavelengths, including the optical forbidden lines, of [FeII], [OI], [SII], [NII], and even H_2 lines together, may sample the parameters space more completely than individual bands. Such analysis provides a check on diagnostic tools derived from individual wavebands. It also serves as a more reliable approach to infer the physical conditions from emission lines of jets. *Nisini et al.* (2005) was the first to demonstrate such an approach through spectra collected for HH1. Using line ratios from [SII], near-IR and optical [FeII], and [CaII], they found evidence for density stratification. The derived temperature also varied from 8000–11000 K using [FeII] to 11000-20000K using [OI] and [NII]. This result suggests that different lines originate from distinct regions (*Nisini et al*, 2005). The results may be a reflection of the fact that different diagnostics are sensitive to different physical conditions. The electron densities derived are higher than the values obtained by applying the BE technique, while the temperature follows an opposite trend. The combined approach has been applied to only a few cases to date. It may become increasingly more useful as more IR observations are become available, particularly from VLTI/AMBER.

4. RADIO CONTINUUM

Radio jets are elongated, jet-like structures seen on subarcsecond scales near stars of low and intermediate masses (e.g., *Evans et al.*, 1987; *Anglada*, 1996). They show good alignment with large-scale optical jets and outflows, usually identifiable with the youngest deeply embedded stellar objects, and have partial association with optical jets or Herbig-Haro objects. In a few YSO sources such as L1551-IRS5, DG Tau B, and HL Tau, the optical jets trace material on scales of several hundred AU and larger, while small radio jets from ionized material are only present very close to the (projected) bases of the optical jets (*Rodríguez et al.*, 1998; *Rodríguez et al.*, 2003). The emission from low-mass radio jet sources is weak, typically at few mJy level.

The production of mJy radio emission has long been a problem for the theory of jets and winds in low-mass YSOs (*Anglada*, 1996). Previous workers agreed that stellar radiation produced too little ionization to account for the observations (e.g., *Rodríguez et al.*, 1989). *Rodríguez and Cantó* (1983) and *Torrelles et al.* (1985) pointed out that thermalization of a small fraction of kinetic energy of a neutral flow might provide the ionization rates inferred from early radio observations. The role of shock-produced UV radiation has also been investigated (e.g., *Hartmann and Raymond*, 1984; *Curiel et al.*, 1987; *Ghavamian and Hartigan*, 1998). *Ghavamian and Hartigan* (1998) investigated free-free emission from postshock regions that are optically thick at radio frequencies. They computed radio spectra under a variety of shock conditions ($10^3 < n < 10^9$ cm^{-3} and $30 < V < 300$ km/s). *González and Cantó* (2002) obtained thermal radio emission at the mJy level by modeling periodically-driven internal shocks in a spherical wind. The radio free-free emission comes from the working surfaces produced by time-varying ejections. In this model, the emission is variable and optical thickness changes with time. At times, emission may completely disappear. SLGS applied the thermal-chemical model of SGSL to radio jets, with wind parameters suitable for Class I sources. They concluded that UV radiation from the same shocks that heat the X-wind may play a role in the ionization structure of radio jets.

Compared with optical and IR emission, the radio emission suffers the least from dust extinction. This makes the radio free-free emission a powerful diagnostic tool for probing close to sources that are under active accretion (e.g., *Reipurth et al.*, 2002, 2004; *Torrelles et al.*, 2003). The archetype L1551-IRS5 is by far the best studied example. It shows jets in both forbidden lines and radio continua. *Rodríguez et al.* (2003) obtained VLA observations with an angular resolution of 0.″1 (14 AU), and found two radio jets from the now-identified binary (e.g., *Rodríguez et al.*, 1998) at the origins of the larger scale jets observed in both optical and NIR wavelengths (*Fridlund and Liseau*, 1998; *Itoh et al.*, 2000). For comparison with the best available observation, SLGS made an intensity map at 3.6 cm based on a profile like Fig. 1 for an X-wind jet of mass loss rate $1 \times 10^{-6} M_\odot$/yr, similar to that inferred from HI measurements of neutral winds (*Giovanardi et al.*, 2000). The elongated contours show clearly the collimation due to the cylindrically stratified density profiles of electrons which

the free-free emission is sensitive of. The apparent collimation can be traced down to below 10 AU level, beyond which radio observations become unresolved. Contour-by-contour comparisons are possible when the theoretical intensity maps are convolved with the real beams to produce synthetic radio images. Direct comparison with observed radio maps, such as the ones shown in Figure 1 of *Rodríguez et al.* (2003), can yield important constraints on detailed physical processes such as heating and ionization. To produce radio emission at the mJy level through thermal bremsstrahlung, enough mass loss rate is needed. A lightly ionized jet in a light wind would produce a radio emission that is well below the sensitivity of current telescopes and too small to be resolved even with interferometric arrays. The preferential detection of radio jets at mJy level and sub-arcsec scales may be an observational selection effect. Radio continuum observations, particularly at the highest possible resolution, can probe the jet structure near the base in a way that complements the optical and near IR observations.

The fluxes of radio jets are characterized by a small non-negative spectral index, $S_\nu \propto \nu^p$ and $p \geq -0.1$, consistent with a thermal origin in ionized winds. The classic example of an unresolved, constant-velocity, fully-ionized, isothermal, spherical wind has $p = 0.6$. *Reynolds* (1986) showed that $p < 0.6$ occurs for an unresolved, partially opaque flow whose cross section grows more slowly than its length. The index can vary from $p = 2$ for totally opaque emission to $p = -0.1$ for totally transparent emission. Observers have usually interpreted radio data with Reynolds' model, obtaining the spectral index from total flux measurements at several wavelengths (e.g., *Rodríguez*, 1998). A more detailed analysis is now possible employing the approaches developed in Section 2. A relation of S_ν-ν performed on X-wind models with self-consistent heating and ionization can best illustrate the behavior at various mass loss rates. For mass loss rates lower than $3 \times 10^{-7} M_\odot \mathrm{yr}^{-1}$, $S_\nu \propto \nu^{-0.1}$, indicating transparent emission. The spectra turn over around 8.3 GHz as the mass loss rate increases to $\dot{M}_w \approx 3 \times 10^{-7} M_\odot \mathrm{yr}^{-1}$, suggesting at this mass loss rate emission from optically thick region starts to appear. For mass loss rates higher than the "cross-over" mass rate $\dot{M}_w$, the index is approximately 0.3–which is very close to what has been inferred for L1551. The value also matches that predicted for a collimating partially optically-thin wind that is lightly ionized.

5. EMISSION FROM INNER DISK WINDS

On general energetic grounds, the fast-moving jets and winds observed in YSOs, if driven magnetocentrifugally, are expected to come from a disk region close to the central object. X-winds automatically satisfy this requirement. For disk-winds to reach a typical speed of a few hundred km/s, they would most likely be launched from the inner disk region, perhaps close to the disk truncation or corotation radii. The dynamics of inner disk-driven winds will be reviewed in the Section 5 (see also the chapter by *Pudritz et al.*). Here, we concentrate on the effort in modeling emission from inner disk-winds, which parallels that described above for X-winds.

To date, emission modeling of disk winds has been carried out using self-similar solutions. *Garcia et al.* (2001a,b), for example, adopted a self-similar solution from *Ferreira* (1997). They concluded that ambipolar-diffusion heating was able to create a *warm* temperature plateau of 10^4 K as in *Safier* (1993a). However, the electron fraction was an order of magnitude below the typical ranges inferred from observations (*Garcia et al.*, 2001a; *Dougados et al.*, 2003). Even for a relatively large wind mass loss rate of $10^{-6} M_\odot$/yr, the average densities are lower than the inferred values of 10^5 to $\geq 10^6$ cm^{-3} by one order of magnitude at projected distances ≤ 100 AU as in the micro-jets (*Dougados et al.*, 2004). Overall, these so-called *cold* disk wind models were unable to reproduce integrated line fluxes in a large sample of classical T-Tauri stars unless a large amount of additional mechanical heating is included. That heating may produce, however, too high an ionization fraction to be consistent with observations (*O'Brien et al.*, 2003; *Dougados et al.*, 2004). A mechanism is needed to heat the wind efficiently without overproducing ionization. A clue for such a mechanism may come from the line ratios. In the inner regions of the DG Tau and RW Aur micro-jets, curves of moderate shock velocities produced by planar shock models seem to fit the excitation condition best (*Lavalley-Fouquet et al.*, 2000; *Dougados et al.*, 2002). This leads to a conclusion similar to that of SGSL (see Section 2.4): mild internal shocks due to time variability in the ejection process may play a role in generating the required gently varying excitation conditions.

Driven from a range of disk radii, a disk wind is expected to have a range of flow speeds. The variation in speed may account for the coexistence of a high-velocity component (HVC) and low-velocity component (LVC) observed in many sources (*Cabrit et al.*, 1999; *Garcia et al.*, 2001b). In particular, the self-similar disk wind model appears capable of producing the two emission peaks in the position-velocity diagrams (PV) of DG Tau and L1551-IRS. The spatial extents of the LVC emissions exceed, however, the model prediction (e.g., *Pesenti et al.*, 2003; *Pyo et al.*, 2002, 2003, 2005a). The LVC may have a more complicated origin. The observed kinematics were best fit with self-similar solutions in which mass-loaded streamlines are coming out from disk radii of 0.07–1 AU (*Garcia et al.*, 2001b); these are inner disk winds. For the HVC, the overall observed velocity widths seem to be narrower than the model predictions. Some disk-wind models show deceleration of the HVC (due to refocusing of streamlines) that is rarely observed (*Pesenti et al.*, 2003; *Dougados et al.*, 2004). It would be interesting to see whether these discrepancies can be removed when the self-similarity assumption is relaxed.

The X-wind is an intrinsically HVC-dominated wind with a strongly density-collimated jet. The velocity profile extends smoothly to the lower velocity range without apparently distinct peaks of emission in a steady-state model. The detailed shapes and locations of the emission peaks may be further affected by local excitation conditions inside the winds. The general features of the HVC can be modeled in a steady-state X-wind. Some well observed sources such as RW Aur and HL Tau, have a predominant HVC (e.g., *Bacciotti et al.*, 1996; *Pyo et al.*, 2005b). Their observed position-velocity diagrams and images in various lines closely resemble model predictions (Figs. 2 and 3 in *Shang et al.*, 1998; Fig. 4 in SGSL). The much weaker LVC may come from the slight extension into the lower velocities due to the natural broadening in the x-region in real systems (*Shu et al.*, 1994), or may originate in a weaker (and slower) disk wind. The much broader, stronger and extended LVC emissions from L1551 and DG Tau may come from a separate strong disk-wind surrounding the faster X-wind jet. Possible interaction between a disk-wind and X-wind is a topic that deserves future attention.

We note that the X-wind is an integral part of the disk-magnetosphere interaction, which also includes funnel flows onto the stellar surface. Possible connections between the disk-winds and funnel flows, if any, remain to be elucidated.

6. INNER DISK WINDS: SIMULATIONS

Since PPIV, MHD wind launching and early propagation has risen to the main focus of a number of numerical simulations. These simulations generally fall into two categories, depending on how the disk is treated. Some workers include the disk as part of the wind simulation (e.g., *Kudoh et al.*, 2003; *von Rekowski and Brandenburg*, 2004), an approach pioneered by *Uchida and Shibata* (1985). The disk-wind system generally evolves quickly, and the long-term outcome of the simulation is uncertain, at least in the ideal MHD limit. In the presence of magnetic diffusion, steady state solutions can be obtained numerically (*Casse and Keppens*, 2002). These solutions extended the semi-analytic self-similar disk-wind solutions (*Wardle and Königl*, 1993; *Li*, 1995; *Ferreira and Casse*, 2004) into the non-self-similar regime. Other workers have chosen to focus on the wind properties exclusively, treating the disk as a boundary (*Krasnopolsky et al.*, 1999, 2003; *Bogovalov and Tsinganos*, 1999; *Fendt and Čemeljić*, 2002; *Anderson et al.*, 2005a), following the original formulation of *Koldoba et al.* (1995) and *Ouyed and Pudritz* (1997). This approach enables the determination of wind properties from the launching surface to large, observable distances.

The simulation setup of *Krasnopolsky et al.* (2003) is closest to that envisioned in the X-wind theory. The wind is assumed to be launched magnetocentrifugally from a Keplerian disk extending from an inner radius R_i to an outer radius R_o. As the axis is approached, the magnetic field lines are forced to become more and more vertical by symmetry and less and less capable of magnetocentrifugal wind-launching. Thus, a fast, light outflow is injected from the disk surface inside R_i, which may represent either the (coronal) stellar wind or the magnetosphere of the star envisioned in the X-wind theory. Two representative wind solutions, both with $R_i = 0.1$ AU and $R_o = 1.0$ AU, are shown in Fig. 3, after a steady state has been reached. Note that the isodensity contours become nearly parallel to the axis in the polar region at large distances. The wind solution in the lower panels of Fig. 3 has a mass loading that is more concentrated near the inner edge of the Keplerian disk. It resembles the X-wind solution shown in Fig. 1 of *Shang et al.* (1998). This cylindrical density stratification is in agreement with the asymptotic analysis of *Shu et al.* (1995; see also *Matzner and McKee*, 1999), which predicts that the dense, axial "jet" is always surrounded by a more tenuous, wide-angle component.

Anderson et al. (2005a) carried out a parameter study of the large-scale structure of axisymmetric magnetocentrifugal winds launched from inner disks, focusing on the effects of mass loading. They found that, despite different degrees of flow collimation, the terminal speed and magnetic level arm scale with the amount of mass loading roughly as predicted analytically for a radial wind (*Spruit*, 1996). As the mass loading increases, the wind of a given magnetic field distribution changes from a "light" regime, where the field lines remain relatively untwisted up to the Alfvén surface, to a "heavy" regime, where the field is toroidally dominated from large distances all the way to the launching surface. The existence of such heavily loaded winds has implications for mass loss from magnetized accretion disks. Whether they are stable in 3D is an open question.

It has been argued that magnetocentrifugal winds may be intrinsically unstable, at least outside the Alfvén surface, where the magnetic field is toroidally dominated (*Eichler*, 1993). *Lucek and Bell* (1996) studied the 3D stability of a (non-rotating) jet accelerated and pinched by a purely toroidal magnetic field. They found that the m=1 (kink) instability can grow to the point of causing the tip of the jet to fold back upon itself. Their mechanism of jet formation is, however, quite different from the magnetocentrifugal mechanism. *Ouyed et al.* (2003) carried out 3D simulations of cold jets launched magnetically along initially vertical field lines from a Keplerian disk. They found that the jets become unstable beyond the Alfvén surface, but the instability is prevented from disrupting the jet by a self-regulatory process that keeps the Alfvén Mach number close to unity. *Anderson et al.* (2005b) adopted as their base models steady axisymmetric winds driven magnetocentrifugally along open field lines inclined more than 30° away from the rotation axis. They increased the mass loading on one half of the launching surface by a factor of $10^{1/2}$ and decreased that on the other half by the same factor. The strongly perturbed winds settle into a new, non-axisymmetric steady state. There is no evidence for the

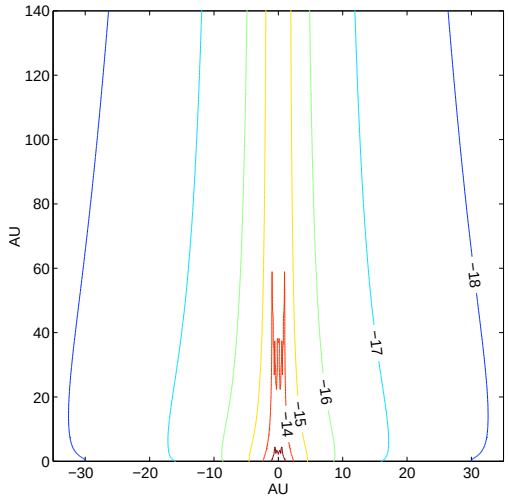

Fig. 2.— Free-free intensity contours (in units erg cm^{-2}s^{-1} str^{-1}) for the X-wind model using parameters scaled up from the SGSL ratio, $L_{\rm X}/\dot{M}_w = 2\times10^{13}$ erg g^{-1}: $\dot{M}_w = 10^{-6}M_\odot{\rm yr}^{-1}$, $L_{\rm X} = 1.3\times10^{33}$ erg s^{-1}, $\alpha = 0.005$, and $\beta = 0$.

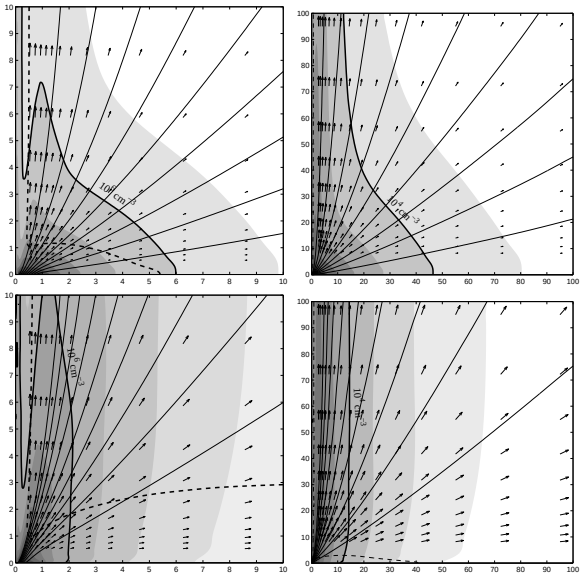

Fig. 3.— Streamlines (light solid) and isodensity contours (heavy solid lines and shades) of two representative steady wind solutions on the 10 AU (left panels) and 10^2 AU (right) scale. The dashed line is the fast magnetosonic surface, and the arrows for poloidal velocity vectors. The wind solution in the lower panels appears better collimated in density. It has a mass loading that is more concentrated near the inner edge of the Keplerian disk.

growth of any instability, even in cases where the magnetic field is toroidally dominated all the way to the launching surface. One possibility is that their magnetocentrifugal winds are stabilized by the strong axial magnetic field enclosed by the wind, as envisioned in *Shu et al.* (1995), although this possibility remains to be firmly established. More discussion of outflow simulations is given in the chapter by *Pudritz et al.*.

7. SIGNATURE OF WIND ROTATION

In the ballistic wind region well outside the fast magnetosonic surface, an approximate relation exists between the poloidal velocity component in the meridian plane $v_{p,\infty}$ and toroidal component $v_{\phi,\infty}$ at a given location (of distance ϖ_∞ from the axis) and the angular speed Ω_0 at the foot point of the magnetic field line passing through that location by (*Anderson et al.*, 2003)

$$\Omega_0 = \frac{v_{p,\infty}^2/2}{v_{\phi,\infty}\varpi_\infty}. \qquad (6)$$

This relation follows from the fact that both the energy and angular momentum in the wind are extracted by the same agent, the magnetic field, from the underlying disk. The angular momentum is extracted by a magnetic torque, which brakes the disk rotation. The energy extracted is simply the work done by the rotating disk against the braking torque (*Spruit*, 1996). To extract more energy out by a given torque, the field lines must rotate faster, which in turn means that they must be anchored closer to the star. At large distances well outside the fast surface, most of the magnetic energy is converted into the kinetic energy of the wind, and most of the angular momentum extracted magnetically will also be carried by fluid rotation. Therefore, the fluid energy and angular momentum at large distances are related through the angular speed at the foot point. Note that all quantities on the right hand side of equation (6) are in principle measurable.

From these measurements, one can deduce the rotation rate at the foot point, and thus the wind launching radius approximately from

$$\varpi_0 = 0.7\left(\frac{\varpi_\infty}{10\ AU}\right)^{2/3}\left(\frac{v_{\phi,\infty}}{10\ {\rm kms}^{-1}}\right)^{2/3} \left(\frac{v_{p,\infty}}{100\ {\rm kms}^{-1}}\right)^{-4/3}\left(\frac{M_*}{1\ M_\odot}\right)^{1/3} AU, \qquad (7)$$

provided that the stellar mass M_* is known independently.

The above technique for locating wind-launching region was applied to the low velocity component of the DG Tau wind, for which detailed velocity field is available from HST/STIS observations (*Bacciotti et al.*, 2000, 2002). These observations allow one to derive not only the line of sight (radial) velocity component but also the rotational velocity. Since the inclination of the flow axis is known for

this source, one can make corrections for the projection effects to obtain the true poloidal and toroidal velocities. The result is shown in Fig. 4. The straight lines connect an observing location where data are available and the location on the disk where we infer the flow in that region originates. One can think of these lines loosely as "streamlines".

The LVC of the DG Tau wind appears to be launched from a region on the disk extending from ~ 0.3 to 4 AU from the central star (the exact range depends somewhat on the distribution of emissivity inside the jet; see *Pesenti et al.*, 2004). That is, the spatially extended, relatively low velocity flow appears to be a disk wind, as has been suspected for some time (*Kwan and Tademaru*, 1988). *Anderson et al.* (2003) have also estimated the so-called "Alfvén radius" along each streamline, which is simply the square root of the specific angular momentum divided by the rotation rate $\varpi_A = (v_{\phi,\infty}\varpi_\infty/\Omega_0)^{1/2}$. It turns out that the Alfvén radius is a factor of 2-3 times the foot point radius (the Alfvén points are indicated by the filled triangles in the figure). This implies that the mass loss rate in the wind is about 10–25% of the mass accretion rate through the disk, if the disk angular momentum removal is dominated by the magnetocentrifugal wind.

There is a high velocity component of more than 200 km s^{-1} in the DG Tau system. It is not spatially resolved in the lateral direction, and is likely originated within 0.3 AU of the star. It could be an X-wind confined by the disk wind. One can in principle use the same technique to infer where the high velocity component originates if its emission can be spatially resolved. This may be achieved through optical interferometers in the future. A potential difficulty is that the highly collimated HVC may be surrounded (and even confined) by an outer outflow (perhaps the LVC), which could mask its rotation signature along the line of sight. The projection effect can create a false impression that the toroidal velocity in a rotating wind increases with the distance from the axis (*Pesenti et al.*, 2004). Also, both the LVC and HVC could be intrinsically asymmetric with respect to the axis, which could create velocity gradients that mimic rotation. This possibility is strengthened by the observation that the disk in RW Aur appears to rotate in the opposite sense to the purported rotation measured in the wind (*Cabrit et al.*, 2005; see also chapter by *Ray et al.*). The apparent rotation signatures should be interpreted with caution (for more discussion, see *Ray et al.*).

8. DENSE CORE ENVIRONMENT

As a wind driven from close to the central stellar object propagates outward, it interacts with the dense core material that is yet to be accreted. To model the interaction properly, one needs to determine the core structure, which depends on how the cores are formed. One school of thought is that the cores are produced by shocks in supersonically turbulent clouds (e.g., *Mac Low and Klessen*, 2004). Although a small fraction of such cores can have subsonic infall motions, the majority expand transonically or even supersonically. The rapid contraction may be difficult to reconcile with the observational results that only a fraction of dense cores show clear evidence for infall and the contraction speeds inferred for the best infall candidates are typically half the sound speed (*Myers*, 1999). Subsonic contraction, on the other hand, is the hallmark of the standard scenario of core formation in magnetically subcritical clouds through ambipolar diffusion (*Nakano*, 1984; *Shu et al.*, 1987; *Mouschovias and Ciolek*, 1999). Predominantly quiescent cores are formed in subcritical clouds even in the presence of strong turbulence (*Nakamura and Li*, 2005). The magnetically-regulated core formation is consistent with Zeeman measurements and molecular line observations of L1544 (*Ciolek and Basu*, 2000), arguably the best observed starless core (*Tafalla et al.*, 1998).

Dynamically important magnetic fields introduce anisotropy to the mass distribution of the core. This anisotropy is illustrated in *Li and Shu* (1996b), who considered the self-similar equilibrium configurations support partly by thermal pressure and partly by static magnetic field. These configurations are described by

$$\rho(r,\theta) = \frac{a^2}{2\pi G r^2} R(\theta);\ \Phi(r,\theta) = \frac{4\pi a^2 r}{G^{1/2}}\phi(\theta), \quad (8)$$

where $R(\theta)$ and $\phi(\theta)$ are dimensionless angular functions of mass density and magnetic flux, respectively. They are solved from the equations of force balance along and across the field direction. The solutions turn out to be a linear sequence of singular isothermal toroids, characterized by a parameter H_0, the fractional over-density supported by the magnetic field above that of supported by thermal pressure. As H_0 increases, the toroid becomes more flattened. These toroids provide plausible initial conditions for protostellar collapse calculations.

Allen et al. (2003a,b) carried out protostellar collapse calculations starting from magnetized singular isothermal toroids, with or without rotation. Examples of non-rotating collapse are shown in Fig. 5 in self-similar coordinates. The dynamical collapse of magnetized toroids proceeds in a self-similar fashion as in the classical non-magnetized (*Shu*, 1977) or strongly magnetized (*Li and Shu*, 1997) limit. Prominent in all collapse solutions of non-zero H_0 is the dense flattened structure in the equatorial region. It is the pseudodisk first discussed in *Galli and Shu* (1993a,b).

For rotating toroids, *Allen et al.* (2003b) concluded that for magnetic fields of reasonable strength, the rotation is braked so efficiently during the protostellar accretion phase that the formation of rotationally supported disks is suppressed in the ideal MHD limit. Non-ideal effects, such as ambipolar diffusion or magnetic reconnection, must be considered for the all-important protostellar disks to appear in the problem of star formation. Most of the angular momentum of the collapsed material is removed by a low-speed wind. Magnetic braking-driven winds have been obtained in the 2D simulations of *Tomisaka* (1998, 2002)

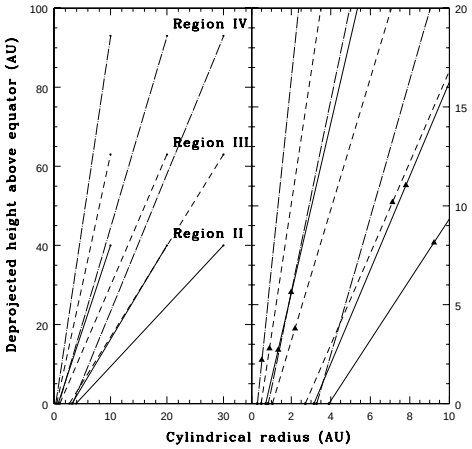

Fig. 4.— Calculated "streamlines" for DG Tau. The left panel shows the observation points from Region II (solid lines), III (dashed), and IV (dash-dotted) of *Bacciotti et al.* (2002) connected to the calculated foot points of the flow. The right is a blow-up of the inner region, showing where the flow originates from the disk. Also shown is the location of the Alfvén surface along each "streamline" as filled triangles.

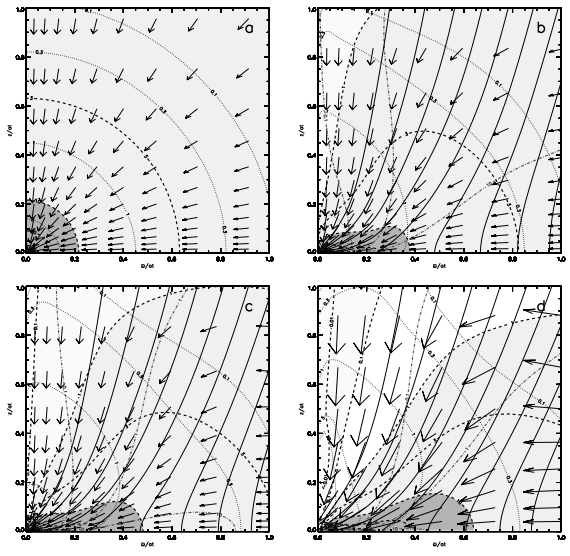

Fig. 5.— Collapse solutions for different degrees of magnetization characterized by $H_0 = 0, 0.125, 0.25, 0.5$. The contours of constant self-similar density $4\pi G t^2 \rho$ are plotted as dashed lines, with the shades highlighting the high density regions. The magnetic field lines are plotted as solid lines, with contours of constant β (ratio of thermal and magnetic pressures; dash-dot-dashed) superposed. Representative velocity vectors are shown as arrows, and dotted lines are contours of constant speed.

and 3D simulations of *Machida et al.* (2004) and *Banerjee and Pudritz* (2005). It is tempting to identify these winds with bipolar molecular outflows. They move, however, too slowly (with a typical speed of a few times the sound speed) to be identified as such. Nevertheless, the slow wind can modify the ambient environment for the fast jet/wind driven from close to the central stellar object, and should be included in a complete theory of molecular outflows. It would be interesting to look for observational signatures of magnetic braking-driven (slow) outflows, perhaps around the youngest protostars.

9. MOLECULAR OUTFLOWS

9.1. Unified Wind-Driven Shell Model

Models for molecular outflows generally fall into two categories: jet-driven and wind-blown (see chapter by *Hector et al.*). The properties of outflows driven by winds were first quantified in *Shu, Ruden, Lada, and Lizano* (1991, hereafter SRLL). It is often stated that the shell model of SRLL is applicable to the class of broad, "classical" CO outflows, but not to the newer class of highly collimated sources (*Bachiller and Tafalla*, 1999). Recent calculations have shown that this need not be the case (*Shang et al.*, 2005, 2006, in preparation). Here, we focus on the advances on the wind-driven shell model since PPIV, starting with a quick overview of the SRLL model.

The SRLL model is characterized by two dimensionless functions, P and Q, that specify the angular distributions of wind momentum per steradian and ambient density

$$\rho(r,\theta) = \frac{a^2}{2\pi G r^2} Q(\theta),\ \frac{\dot{M}_w v_w}{4\pi} P(\theta), \qquad (9)$$

where a is the isothermal sound speed, G the gravitational constant, and $\dot{M}_w$ and v_w represent the mass loss rate and velocity of the wind. If the ambient medium is swept into a thin shell by the wind in a momentum conserving fashion, the angular distribution of the speed, and thus the shape, of the shell is determined by a bipolarity function $\mathcal{B} \propto (P/Q)^{1/2}$.

Current observations are unable to provide detailed information on the functions $P(\theta)$ and $Q(\theta)$. They can be determined theoretically in idealized situations. For example, one can use as the angular distribution $Q(\theta)$ the function $R(\theta)$ in equation (8), which describes the density distribution of a magnetized singular isothermal toroid. This was first done in *Li and Shu* (1996a), who also adopted an idealized angular distribution for wind momentum $P(\theta) \propto 1/\sin^2\theta$ that is motivated by an asymptotic theory of magnetocentrifugal winds (*Shu et al.*, 1995). For a toroid of over-density parameter $H_0 = 0.5$ (which gives an aspect ratio of column density contours of about 2:1, as typically observed in low-mass cores; *Myers et al.*, 1991), the bipolarity function $\mathcal{B}$ corresponds to a shell of hour-glass shape,

with a relatively wide opening near the base. This simple analytic model can explain several features commonly observed in molecular outflows, including mass-velocity relation and Hubble-type expansion. The fact that the shell in the model does not close on itself raises the question of its applicability to relatively young sources whose shells of outflowing material are often observed to be closed.

Shang et al. (2005) reconsidered the above model of molecular outflow formation through numerical simulations. The simulations, carried out using Zeus2D (*Stone and Norman*, 1992), allowed them to relax some of the simplifying assumptions made in the analytic models. Examples of the numerically computed shells are shown in Fig. 6. These are obtained by running a cylindrically stratified, toroidally magnetized wind of Alfvén Mach number 6 into toroids of different degrees of flattening, characterized by the over-density parameter $H_0 = 0.25, 0.5, 1.0,$ and 1.5. Common to all cases is the apparent two-component density structure: a dense axial jet, which is part of the primary wind, and a dense, closed, shell, which encases the jet. Between the jet and shell lies the wide-angle wind.

Note that the same density-stratified wind produces shells of varying degrees of collimation, some of which are jet-like. The jet-like shells are produced in relatively weakly magnetized toroids (with values of H_0 less than unity), which have a relatively narrow low-density polar funnel through which the primary wind escapes. Even in more strongly magnetized toroids, the shells are still significantly elongated, despite the fact that the density distribution in the ambient toroids is strongly flattened. The elongation is due, to a large extent, to the anisotropy in the momentum distribution intrinsic to the shell-driving primary wind. In this picture, both the dense, axial "jet" part of the wind and the more tenuous "wide-angle" component participate in shaping the shell structure: the jet controls the length of the shell and the wide-angle component (together with the lateral ambient density distribution) the width. The jet-driven and wind-blown scenarios are thus unified in the single framework of SRLL, which appears capable of producing both classical and jet-like molecular outflows. In particular, the fast SiO jets observed in the prototype of jet-like outflows, HH211, find a natural explanation in this unified model (see Section 9). The flattened NH_3 core, elongated CO shell, and highly collimated H_2 jet observed in HH212 (*Lee et al.*, 2006) also strongly resemble the prominent features shown in Fig. 5.

Dynamical collapse is expected to modify the ambient environment through which the primary wind propagates, particularly near the central star (see Fig. 5). A future refinement of the shell model of SRLL would be to include the collapse-induced modification to the ambient density distribution, which is expected to broaden the base of the wind-driven cavity, especially at late times, when the collapsing region has expanded to large distances. The evolution of the collapsing envelope may be a key factor in controlling the outflow evolution from Class 0 to Class I to Class II described in *Arce et al.*. Indeed, one may heuristically view the sequence of models with increasing degrees of toroid flattening in Fig. 6 as an evolutionary sequence in time: as the collapse empties out an increasingly larger region near the star, the outflow cavity becomes wider near the base in time.

Another improvement would be in treating the wind-ambient interface, where mixing is expected due to Kelvin-Helmholtz instability. *Cunningham et al.* (2005) treated the interface using Adaptive Mesh Refinement (AMR) techniques, extending the work of *Gardiner et al.* (2003) by including molecular, ionic and atomic species, cooling functions and molecule recombination and dissociation. They were able to partially resolve the strongly cooling, shocked layers around the outflow lobes. They found that the shocked wind and ambient medium are not completely mixed along the walls of the wind-blown cavity, but noted that this result might be affected by their limited resolution, despite the fact that AMR was used.

9.2. HH211 and SiO Emission

As mentioned earlier, the wind-driven shell model was thought to be unable to explain the class of highly-collimated molecular outflows. It turns out, however, that the prototype of the class, HH211, may have structures that most closely correspond to the predictions of the unified shell model.

The HH211 outflow in the IC 348 molecular cloud complex (D$\sim$315 pc) was discovered in the NIR H_2 emission (*McCaughrean et al.*, 1994). It is driven by a low-luminosity (3.6 $L_\odot$) Class 0 protostar and is considered to be extremely young, with a dynamical age of only $\sim$750 yr. The high-resolution ($1.5''$) CO J=2–1 observations by *Gueth and Guilloteau* (1999) revealed a remarkable structure: the low-velocity CO delineates a pair of shells whose tips are associated with NIR H_2 emission, while the high-velocity CO traces a narrower feature whose velocity increases linearly with distance from the star. PV diagrams of the CO emission show parabolic shapes characteristic of wind-driven shells (*Lee et al.*, 2000). It is plausible that the CO emission traces a shell of ambient material swept up by a (wide-angle) primary wind.

Bisecting the CO lobe is a narrow jet of thermal SiO emission. The thermal emission from SiO is considered to trace the dense shocked gas because its extremely low gas-phase abundance ($< 10^{-12}$) in quiescent regions (*Ziurys et al.*, 1989; *Martín-Pintado et al.*, 1992) can be enhanced by several orders of magnitude by means of shocks. The SiO emission is detected in J=1–0 (*Chandler and Richer*, 2001), J=5–4 (*Gibb et al.*, 2004), 8–7 and 11–10 (*Nisini et al.*, 2002b). Since some of these lines have critical densities higher than $\sim 10^6$ cm^{-3} and the energy level of J=11 is higher than 100 K, their detection means that the SiO jet is much denser and warmer than the lower-velocity shell component. High resolution (1–$2''$) observations of SiO J=8–7 (*Palau et al.*, 2006), 5–4 (*Hirano et al.*, 2006a), and 3–2 (*Hirano et al.*, 2006b, in preparation) have been done using

SMA and NMA. As shown in Fig. 7, the SiO jet is resolved into a chain of knots separated by $4''$ ($\sim$1000 AU). The SiO knots have their H_2 counterparts except the ones in close vicinity of the central source where the extinction is large. The knotty structure is more prominent in the higher SiO transition. The innermost knots located at $\pm 2''$ from the source are prominent in the J=8–7 and 5–4 maps, while barely seen in the J=1–0 map. *Hirano et al.* (2006a) estimated that these knots have a temperature $>$300–500 K and density (0.5–1)$\times 10^7$ cm^{-3}. These densities and temperatures are much higher than those inferred for the CO shell component, indicating that the SiO jet has a different origin. The most likely possibility is that the SiO jet traces the densest part of the primary wind. This identification is strengthened by the PV diagrams of SiO J=8–7 and 5–4 emission (Fig. 8), which show a large (projected) velocity dispersion ($\sim$ 30 km s^{-1}) close to the star. This velocity feature, absent from the CO emission, is reminiscent of that predicted in the X-wind theory for optical forbidden lines (*Shang et al.*, 1998). It may be indicative of a (perhaps unsteady) wide-angle wind that is stratified in density, as envisioned in our unified model of molecular outflows.

The spectacular SiO jet of HH211 is not unique. It is seen in at least one other young Class 0 source, L1448mm (*Bachiller et al.*, 1991; *Guilloteau et al.*, 1992; *Dutrey et al.*, 1997). The SiO abundance is estimated to be $\sim 10^{-6}$ (*Martín-Pintado et al.*, 1992; *Bachiller et al.*, 1991; *Hirano et al.*, 2006a) in both L1448mm and HH211, implying an enhancement by a factor of $\geq 10^5$ above the value in the ambient quiescent clouds. The bright SiO jet appears to fade away quickly as the source evolves. SiO emission is also observed at the tips of outflow cavities in some sources, including L1527 (*Mikami et al.*, 1992; *Zhang et al.*, 1995, 2000; *Gueth et al.*, 1998; *Bachiller et al.*, 2001), IRAS 03282 (*Bachiller et al.*, 1994), BHR71 (*Garay et al.*, 1998), and NGC 1333 IRAS 2A (*Jørgensen et al.*, 2004). For these sources, the typical SiO abundance is $\sim 10^{-9}$–10^{-8} (e.g., *Bachiller*, 1996). Narrow SiO lines have been detected in relatively quiescent regions around SVS 13 (*Lefloch et al.*, 1998; *Codella et al.*, 1999), B1 (*Martín-Pintado et al.*, 1992; *Yamamoto et al.*, 1992), IRAS 00338+6312, and Cep A (*Codella et al.*, 1999). The estimated SiO abundance is about 10^{-11}–10^{-10} (*Lefloch et al.*, 1998; *Codella et al.*, 1999), the lowest among the three classes described here. These three classes of SiO sources can plausibly be put into an evolutionary sequence (*Bachiller and Tafalla*, 1999). Detailed calculations that take into account the evolution of both the primary wind and the ambient medium, as well as SiO chemistry, are needed to quantify the sequence. The unified wind-driven shell model provides a framework for quantifying the outflow evolution.

10. CONCLUDING REMARKS

We have reviewed the progress on the X-wind model and related work since PPIV. In particular, we showed that when detailed excitation conditions and radiative processes are modeled, X-winds are capable of explaining the gross characteristics of many observations, ranging from optical forbidden lines to thermal radio emission. To make model predictions match observational data, a mechanical heating is required to keep the wind warm enough to emit in optical and radio. The heating is prescribed phenomenologically, and may be related to wind variabilities, which produce shocks of varying strengths. How the variabilities are generated remains little explored, and should be a focus of future investigation.

Dynamical models of jets and winds in YSOs have shown some convergence. The magnetocentrifugal mechanism remains the leading candidate for outflow production. The modeling effort is hampered, however, by our limited knowledge of the physical conditions near the wind-disk interface. These include both the thermal and ionization structure of the region, as well as the magnetic field distribution. Detailed calculations that treat the coupling between the wind, the disk, and perhaps the stellar magnetosphere self-consistently may unify the disk-wind and X-wind picture. An improved model of the jets and winds will also deepen our understanding of the molecular outflows that they drive.

Acknowledgments.

The authors would like to thank the referee for his careful reading and thorough review of the manuscript. This work is supported by the Theoretical Institute for Advanced Research in Astrophysics (TIARA) operated under Academia Sinica and the National Science Council Excellence Projects program in Taiwan administered through grant number NSC 94-2752-M-007-001, and NSC92-2112-M-007-051, and NASA grant NAG5-12102 and NSF AST-0307368 in USA.

REFERENCES

Allen A., Li Z.-Y., and Shu F. H. (2003a) *Astrophys. J., 599*, 351-362.

Allen A., Li Z.-Y., and Shu F. H. (2003b) *Astrophys. J., 599*, 363-379.

Anderson J. M., Li Z.-Y., Krasnopolsky R., and Blandford R. D. (2003) *Astrophys. J., 590*, L107-L110.

Anderson J. M., Li Z.-Y., Krasnopolsky, R., and Blandford, R. D. (2005a) *Astrophys. J., 630*, 945-957.

Anderson J. M., Li Z.-Y., Krasnopolsky, R., and Blandford, R. D. (2005b) *PPV Poster Proceedings* http://www.lpi.usra.edu/meetings/ppv2005/pdf/8499.pdf

Anglada G. (1996) in *Radio Emission From The Stars and The Sun*, (A. R. Taylor and J. M. Paredes, eds.), pp.3-14. ASP Conference Series, San Francisco.

Bacciotti F. (2002) *Rev. Mex. Astron. Astrofis. (Serie de Conferencias), 13*, 8–15.

Bacciotti F., and Eislöffel J. (1999) *Astron. Astrophys., 342*, 717–735. (*BE*)

Bacciotti F., Hirth G. A., and Natta A. (1996) *Astron. Astrophys., 310*, 309-314.

Bacciotti F., Mundt R., Ray T. P., Eislöffel J., Solf J., and Camezind M. (2000) *Astrophys. J., 537*, L49–L52.
Bacciotti F., Ray T. P., Mundt R., Eislöffel J., and Solf J. (2002) *Astrophys. J., 576*, 222–231.
Bachiller R. (1996) *Ann. Rev. Astron. Astrophys., 34*, 111-154.
Bachiller R. and Tafalla M. (1999) In *The Origin of Stars and Planetary Systems* (C. J. Lada and N. D. Kylafis eds.), pp. 227-266. Kluwer Academic Publishers.
Bachiller R., Martín-Pintado J., and Fuente A. (1991) *Astron. Astrophys., 243*, L21-L24.
Bachiller R., Terebey S., Jarrett T., Martín-Pintado J., Beichman C. A., and van Buren D. (1994) *Astrophys. J., 437*, 296-304.
Bachiller R., Pérez Gutiérrez M., Kumar M. S. N., and Tafalla M. (2001) *Astron. Astrophys. 372*, 899-912.
Banerjee R. and Pudritz R. E. (2005) *PPV Poster Proceedings* http://www.lpi.usra.edu/meetings/ppv2005/pdf/8117.pdf
Binette L., Cabrit S., Raga A., and Cantó J. (1999) *Astron. Astrophys., 346*, 260-266.
Blandford R. D. and Payne D. G. (1982) *Mon. Not. R. Astron. Soc., 199*, 883-903.
Bogovalov S. and Tsinganos K. (1999) *Mon. Not. R. Astron. Soc., 305*, 211-224.
Cabrit S., Ferreira J., and Raga A. C. (1999) *Astron. Astrophys., 343*, L61-L64.
Cabrit S., Pety J., Pesenti N. and Dougados C (2005) *PPV Poster Proceedings* http://www.lpi.usra.edu/meetings/ppv2005/pdf/8103.pdf
Casse F. and Keppens R. (2002) *Astrophys. J., 581*, 988-1001.
Chandler C. J. and Richer J. S. (2001) *Astrophys. J., 555*, 139-145.
Ciolek G. E. and Basu S. (2000) *Astrophys. J., 529*, 925-931.
Codella C., Bachiller R., and Reipurth B. (1999) *Astron. Astrophys., 343*, 585-598.
Cunningham A., Frank A., and Hartmann L. (2005) *Astrophys. J., 631*, 1010-1021.
Curiel S., Cantó J., and Rodríguez L. F. (1987) *Rev. Mex. Astron. Astrofis., 14*, 595–602.
Davis C. J., Whelan E., Ray T. P., and Chrysostomou A. (2003) *Astron. Astrophys., 397*, 693–710.
Dougados C., Cabrit S., Lavalley C., and Ménard F. (2000) *Astron. Astrophys., 357*, L61-L64.
Dougados C., Cabrit S., and Lavalley-Fouquet C. (2002) *Rev. Mex. Astron. Astrofis. Ser. Conf., 13*, 43-48.
Dougados C., Cabrit S., López-Martín L., Garcia P., and O'Brien, D. (2003) *Astrophys. Space Sci., 287*, 135-138.
Dougados C., Cabrit S., Ferreira J., Pesenti N., Garcia P., and O'Brien D. (2004) *Astrophys. Space Sci., 293*, 45-52.
Draine B. T. (1980) *Astrophys. J., 241*, 1021-1038.
Dutrey A., Guilloteau S., and Bachiller R. (1997) *Astron. Astrophys., 325*, 758-768
Eichler D (1993) *Astrophys. J., 419*, 111-116.
Evans N. J. II, Levreault R. M., Beckwith S., and Skrutskie M. (1987) *Astrophys. J. 320*, 364-375.
Feigelson E. D. and Montmerle T. (1999) *Ann. Rev. Astron. Astrophys., 37*, 363–408.
Feigelson E. D., Broos P., Gaffney J. A. III, Garmire G., Hillenbrand L. A., Pravdo S. H., Townsley L., and Tsuboi Y. (2002) *Astrophys. J., 574*, 258–292.
Feigelson E. D., Getman K., Townsley L., Garmire G., Preibisch T., Grosso N., Montmerle T., Muench A., and McCaughrean M. (2005) *Astrophys. J. Suppl., 160*, 379–389.
Fendt C. and Čemeljić M. (2002) *Astron. Astrophys., 395*, 1045-1060.
Ferreira J. (1997) *Astron. Astrophys., 319*, 340-359.
Ferreira J. and Casse F. (2004) *Astrophys. Space Sci., 292*, 479-492.
Fridlund C. V. M. and Liseau R. (1998) *Astrophys. J., 499*, L75-L77.
Galli D. and Shu F. (1993a), *Astrophys. J. 417*, 220-242.
Galli D. and Shu F. (1993b), *Astrophys. J. 417*, 243-258.
Garay G., Köhnenkamp I., Bourke T. L., Rodríguez L. F., and Lehtinen K. K. (1998) *Astrophys. J., 509*, 768-784.
Garcia P. J. V., Ferreira J., Cabrit S., and Binette L. (2001a) *Astron. Astrophys., 377*, 589-608.
Garcia P. J. V., Cabrit S., Ferreira J., and Binette L. (2001b) *Astron. Astrophys., 377*, 609-616.
Gardiner T. A., Frank A., and Hartmann L. (2003) *Astrophys. J., 582*, 269-276.
Ghavamian P. and Hartigan P. (1998) *Astrophys. J., 501*, 687-698.
Gibb A. G., Richer J. S., Chandler C. J., and Davis C. J. (2004) *Astrophys. J., 603*, 198-212.
Giovanardi C., Rodríguez L. F., Lizano S., and Cantó J. (2000) *Astrophys. J., 538*, 728-737.
González R. F. and Cantó J. (2002) *Astrophys. J., 580*, 459-467.
Glassgold A. E., Najita, J., and Igea J. (1997) *Astrophys. J., 480*, 344-350.
Glassgold A. E., Feigelson E. D., and Montmerle T. (2000) In *Protostars and Planets IV* (V. Mannings et al., eds.), pp. 429-456. Univ. of Arizona, Tucson.
Glassgold A. E., Krstić P. S., and Schultz D. R. (2005a) *Astrophys. J., 621*, 808-816.
Glassgold A. E., Feigelson E. D., Montmerle T., and Wolk, S. (2005b) in *Chondrites and the Protoplanetary Disk* (A. N. Krot et al., eds.), pp. 165-180. ASP Conference Series, San Francisco.
Grosso N., Montmerle T., Feigelson E. D., Andre P., Casanova S., and Gregorio-Hetem J. (1997) *Nature, 387*, 56-58.
Gueth F. and Guilloteau S. (1999) *Astron. Astrophys., 343*, 571-584.
Gueth F., Guilloteau S., and Bachiller R. (1998) *Astron. Astrophys., 333*, 287-297.
Guilloteau S., Bachiller R., Fuente A., and Lucas R. (1992) *Astron. Astrophys., 265*, L49-L52.
Hartigan P., Morse J. A., and Raymond J. (1994) *Astrophys. J., 436*, 125-143.
Hartigan P, Raymond J., and Pierson R. (2004) *Astrophys. J., 614*, L69–L71.
Hartmann L. and Raymond J. C. (1984) *Astrophys. J., 276*, 560-571.
Hirano N., Liu S.-Y., Shang H., Ho P. T. P., Huang H.-C., Kuan Y.-J., McCaughrean M. J., and Zhang Q. (2006a) *Astrophys. J., 636*, L141-L144.
Itoh Y., Kaifu N., Hayashi M., Hayashi S. S., Yamashita T., Usuda T., Noumaru J., Maihara T., Iwamuro F., Motohara K., Taguchi T., and Hata R. (2000) *Publ. Astron. Soc. Japan, 52*, 81-86.
Jørgensen J. K., Hogerheijde M. R., Blake G. A., van Dishoeck E. F., Mundy L. G., Schöier F. L. (2004) *Astron. Astrophys., 415*, 1021-1037.
Koldoba A. V., Ustyugova G. V., Romanova M. M., Chechetkin V. M., and Lovelace R. V. E. (1995) *Astrophys. Space Sci., 232*, 241-261.
Königl A. and Pudritz R. E. (2000) In *Protostars and Planets IV* (V. Mannings et al., eds.), pp. 759-788. Univ. of Arizona, Tucson.
Krasnopolsky R., Li Z.-Y., and Blandford R. (1999) *Astrophys. J.,*

526, 631-642.
Krasnopolsky R., Li Z.-Y., and Blandford R. (2003) *Astrophys. J., 595*, 631-642.
Krstić P. S. and Schultz D. R. (1998), *Atomic and Plasma-Material Data for Fusion, 8*.
Kudoh T., Matsumoto R., and Shibata K. (2003) *Astrophys. Space Sci., 287*, 99-102.
Kwan J. and Tademaru E. (1988) *Astrophys. J., 332*, L41-L44.
Lavalley-Fouquet C., Cabrit S., and Dougados C. (2000) *Astron. Astrophys., 356*, L41-L44.
Lee C.-F., Mundy L. G., Reipurth B., Ostriker E. C. and Stone J. M. (2000) *Astrophys. J. 542*, 925-945.
Lee C.-F., Ho P. T. P., Beuther H., Bourke T. L., Zhang Q., Hirano N., and Shang H. (2006) *Astrophys. J.*, in press; astro-ph/0511059
Lefloch B., Castets A., Cernicharo J., and Loinard L. (1998) *Astrophys. J., 504*, L109-L112.
Li Z.-Y. (1995) *Astrophys. J., 444*, 848-860.
Li Z.-Y. and Shu F. H. (1996a), *Astrophys. J., 468*, 261-268.
Li Z.-Y. and Shu F. H. (1996b) *Astrophys. J., 472*, 211-224.
Li Z.-Y. and Shu F. H. (1997) *Astrophys. J., 475*, 237-250.
Lucek S. G. and Bell A. R. (1996) *Mon. Not. Roy. Astron. Soc., 281*, 245-256.
Mac Low M.-M. and Klessen R. S. (2004)*Rev. Modern Phys., 76*, 125-194.
Machida M. N., Tomisaka K., and Matsumoto T. (2004) *Mon. Not. R. Astron. Soc., 348*, L1–L5.
Martín-Pintado J., Bachiller R., and Fuente A. (1992) *Astron. Astrophys., 254*, 315-326.
Matzner C. D. and McKee C. F. (1999) *Astrophys. J., 526*, L109-L112.
McCaughrean M. J., Rayner J. T., and Zinnecker H. (1994) *Astrophys. J., 436*, L189-L192.
Mikami H., Umemoto T., Yamamoto S., and Saito S. (1992) *Astrophys. J., 392*, L87-L90.
Mouschovias T. Ch. and Ciolek G. E. (1999) In *The Origin of Stars and Planetary Systems* (C. J. Lada and N. D. Kylafis eds.), pp. 305-340. Kluwer Academic Publishers.
Myers P. C. (1999) In *The Origin of Stars and Planetary Systems* (C. J. Lada and N. D. Kylafis eds.), pp. 67-96. Kluwer Academic Publishers.
Myers P.C., Fuller, G.A., Goodman, A.A., and Benson, P.J. (1991) *Astrophys. J., 376*, 561-572
Nakamura F. and Li Z.-Y. (2005) *Astrophys. J., 631*, 411-428.
Nakano T. (1984) *Fundamentals of Cosmic Physics, 9*, 139-231.
Nisini B., Caratti o Garatti A., Giannini T., and Lorenzetti D. (2002a) *Astron. Astrophys., 393*, 1035-1051
Nisini B., Codella C., Giannini T., and Richer J. S. (2002b) *Astron. Astrophys., 395*, L25-L28.
Nisini B., Bacciotti F., Giannini T., Massi F., Eislöffel J., Podio L., and Ray T. P. (2005) *Astron. Astrophys., 441*, 159-170.
O'Brien D., Garcia P., Ferreira J., Cabrit S., and Binette L. (2003) *Astrophys. Space Sci., 287*, 129-134.
Osterbrock D. E. (1961) *Astrophys. J., 134*, 270-272.
Ouyed R. and Pudritz R. E. (1997) *Astrophys. J., 482*, 712-732.
Ouyed R., Clarke D. A., and Pudritz R. E. (2003) *Astrophys. J., 582*, 292-319.
Palau A., Ho P. T. P., Zhang Q., Estalella R., Hirano N., Shang H., Lee C.-F., Bourke T. L., Beuther H., and Kuan Y.-J. (2006) *Astrophys. J., 636*, L137-L140.
Pesenti N., Dougados C., Cabrit S., O'Brien D., Garcia P., and Ferreira J. (2003) *Astron. Astrophys., 410*, 155-164.
Pesenti N., Dougados C., Cabrit S., Ferreira J., Casse F., Garcia P., and O'Brien D. (2004) *Astron. Astrophys., 416*, L9-L12.
Pradhan A. K. and Zhang H. L. (1993)*Astrophys. J., 409*, L77-L79.
Pyo T.-S., Hayashi M., Kobayashi N., Terada H., Goto M., Yamashita T., Tokunaga A. T., and Itoh Y. (2002) *Astrophys. J., 570*, 724-733.
Pyo T.-S., Kobayashi N., Hayashi M., Terada H., Goto M., Takami H., Takato N., Gaessler W., Usuda T., Yamashita T., Tokunaga A. T., Hayano Y., Kamata Y., Iye M., and Minowa Y. (2003) *Astrophys. J., 590*, 340-347.
Pyo T.-S., Hayashi M., Kobayashi N., Tokunaga A. T., Terada H., Tsujimoto M., Hayashi S. S., Usuda T., Yamashita T., Takami H., Takato N., and Nedachi K. (2005a) *Astrophys. J., 618*, 817-821.
Pyo T.-S., Hayashi M., Kobayashi N., Terada H., and Tokunaga A. T. (2005b) *J. Korean Astron. Soc., 38*, 249-252.
Raga A. C., Böhm K.-H., and Cantó J. (1996) *Rev. Mex. Astron. Astrofis., 32*, 161-174.
Ray T. P. and Bacciotti F. (2003) *Rev. Mex. Astron. Astrofis. Ser. Conf., 15*, 106-111.
Reipurth B., Yu K. C., Heathcote S., Bally J., and Rodríguez L. F. (2000) *Astron. J., 120*, 1449-1466.
Reipurth B., Rodríguez L. F., Anglada G., and Bally J. (2002) *Astrophys. J. 125*, 1045-1053.
Reipurth B., Rodríguez L. F., Anglada G., and Bally J. (2004) *Astrophys. J. 127*, 1736-1746.
Reynolds S. P. (1986) *Astrophys. J., 304*, 713–720.
Rodríguez L. F. (1998) *Rev. Mex. Astron. Astrofis., 7*, 14-20.
Rodríguez L. F. and Cantó J. (1983) *Rev. Mex. Astron. Astrofis., 8*, 163-173.
Rodríguez L. F., Myers P. C., Cruz-González I., and Terebey S. (1989) *Astrophys. J., 347*, 461-467.
Rodríguez L. F., D'Alessio P., Wilner D. J., Ho P. T. P., Torrelles J. M., Curiel S., Gómez Y., Lizano S., Pedlar A., Cantó J., and Raga A. C. (1998) *Nature, 395*, 355-357.
Rodríguez L. F., Porras A., Claussen M. J., Curiel S., Wilner D. J., and Ho Paul T. P. (2003) *Astrophys. J., 586*, L137-L139.
Ruden S. P., Glassgold A. E., and Shu F. H. (1990) *Astrophys. J., 361*, 546-569. (*RGS*)
Safier P. N. (1993a) *Astrophys. J., 408*, 115-147.
Safier P. N. (1993b) *Astrophys. J., 408*, 148-159.
Shang H., Shu F. H., and Glassgold A. E. (1998) *Astrophys. J., 493*, L91-L94.
Shang H., Glassgold, A. E., Shu, F. H., and Lizano, S. (2002) *Astrophys. J., 564*, 853-876. (*SGSL*)
Shang H., Lizano S., Glassgold A. E., and Shu F. (2004) *Astrophys. J., 612*, L69-L72. (*SLGS*)
Shang H., Allen A., Liu C.-F., Li Z.-Y., Chou M.-Y. and Anderson J. (2005) *AAS 207*, #163.06
Shu F. H. (1977) *Astrophys. J., 214*, 488-497.
Shu F. H. (1992) *The Physics of Astrophysics: Gas Dynamics, Volume II*. University Science Books, Herndon.
Shu F. H., Adams F. C., and Lizano S. (1987) *Ann. Rev. Astron. Astrophys., 25*, 23-81.
Shu F. H., Ruden S. P., Lada C. J., and Lizano S. (1991) *Astrophys. J., 370*, L31-L34. (*SRLL*)
Shu F., Najita J., Ostriker E., Wilkin F., Ruden S., and Lizano S. (1994), *Astrophys. J., 429*, 781-796.
Shu F. H., Najita J., Ostriker E. C., and Shang H. (1995) *Astrophys. J., 455*, L155-L158.
Shu F. H., Shang H., Glassgold A. E., and Lee T. (1997) *Science,*

277, 1475-1479.
Shu F. H., Najita J. R., Shang H., and Li Z.-Y. (2000) In *Protostars and Planets IV* (V. Mannings, A. P. Boss, and S. S. Russell, eds.), pp. 789-814. Univ. of Arizona, Tucson.
Spruit H. C. (1996) In *Evolutionary Processes in Binary Stars* (R. A. M. J. Wijers et al., eds.), pp. 249-286. Kluwer Academic Publishers, Dordrecht.
Stone J. M. and Norman M. L. (1992) *Astrophys. J. Suppl., 80*, 791-818.
Tafalla M., Mardones D., Myers P. C., Caselli P., Bachiller R., and Benson P. J. (1998) *Astrophys. J., 504*, 900-914.
Tomisaka K. (1998) *Astrophys. J., 502*, L163-L167.
Tomisaka K. (2002) *Astrophys. J., 575*, 306-326.
Torrelles J. M., Ho P. T. P., Rodríguez L. F., and Cantó J. (1985) *Astrophys. J., 288*, 595-603.
Torrelles J. M., Cantó J., Rodríguez L. F., Ho P. T. P. and Moran J. M. (1985) *Astrophys. J. 294*, L117-L120.
Torrelles J. M., Patel N. A., Anglada G., Gómez J. F., Ho P. T. P., Lara L., Alberdi A., Cantó J., Curiel S., Garay G., and Rodríguez L. F. (2003) *Astrophys. J. 598*, L115-L119.
Tsuboi Y., Imanishi K., Koyama K., Grosso N., and Montmerle T. (2000) *Astrophys. J., 532*, 1089-1096.
Uchida Y. and Shibata K. (1985) *Publ. Astron. Soc. Japan, 37*, 515-535.
Verner E. M., Verner D. A., Baldwin J. A., Ferland G. J., and Martin P. G. (2000) *Astrophys. J., 543*, 831-839.
von Rekowski B. and Brandenburg A. (2004) *Astron. Astrophys., 420*, 17-32.
Wardle M. and Königl A. (1993) *Astrophys. J., 410*, 218-238.
Yamamoto S., Mikami H., Saito S., Kaifu N., Ohishi M., and Kawaguchi K. (1992) *Publ. Astron. Soc. Japan, 44*, 459-467.
Zhang H. L. and Pradhan A. K. (1995) *Astron. Astrophys., 293*, 953-966.
Zhang Q., Ho P. T. P., Wright M. C. H., and Wilner D. J. (1995) *Astrophys. J., 451*, L71-L74.
Zhang Q., Ho P. T. P., and Wright M. C. H. (2000) *Astron. J., 119*, 1345-1351.
Ziurys L. M., Friberg P., and Irvine W. M. (1989) *Astrophys. J., 343*, 201-207.

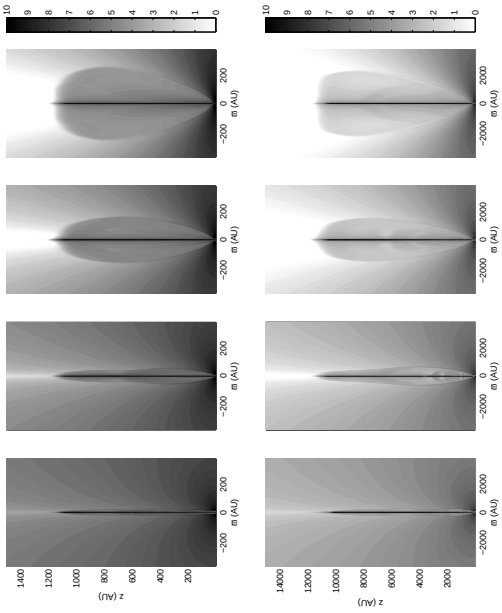

Fig. 6.— Snapshots of density structures at 100 (top) and 1000 (bottom) years for a wind of mass loss rate ($1 \times 10^{-6} M_{\odot}$/yr) and Alfvén Mach number 6. The toroids are shown in the order of $H_0 = 0.25$, 0.5, 1, and 1.5 (from left to right). The color bar shows density variation in logarithmic (log_{10}) scale.

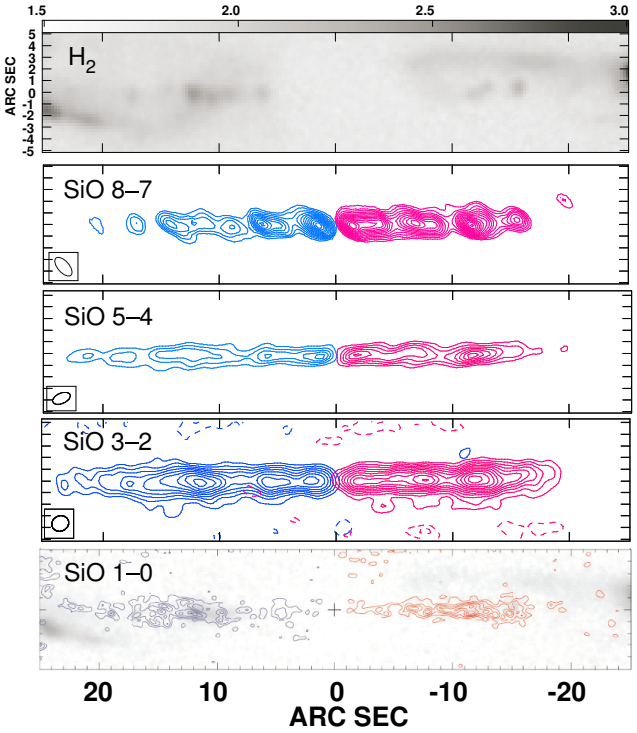

Fig. 7.— HH211 outflow observed with the near-infrared H_2 $v = 1 - -0$ S(1) emission (grey scale in the top panel; *Hirano et al.*, 2006a) and the SiO J=8–7 (*Palau et al.*, 2006), J=5–4 (*Hirano et al.*, 2006a), J=3–2 (*Hirano et al.*, 2006b, in prep.), and J=1–0 (*Chandler & Richer*, 2001). All the images are rotated by $-26°$ from the equatorial coordinates. The contours represent the integrated SiO emission in the blueshifted velocity range (positive offset from the position of the driving source, HH211-mm, along the major axis) and in the redshifted velocity range (negative offset).

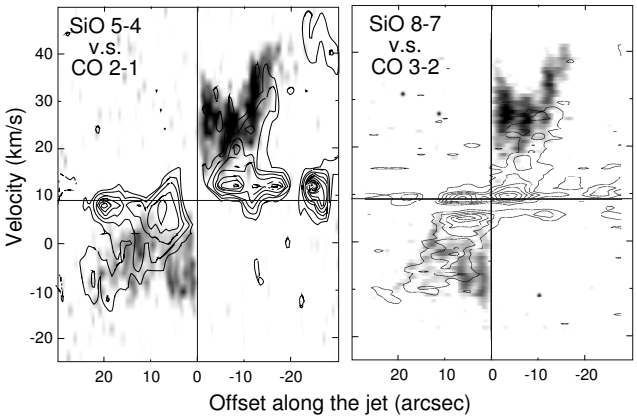

Fig. 8.— Position-velocity (p-v) plots of the SiO and CO along the major axis of the HH211 outflow. *Left:* The SiO J=5–4 (grey scale) superposed on the CO J=2–1 (contours from *Gueth and Guilloteau*, 1999) *Right:* The SiO J=8–7 (grey scale) and the CO J=3–2 (contours) from *Palau et al.*, (2006). The vertical and horizontal straight lines indicate the position of the continuum source and the systemic velocity, respectively.